MDPI

Article

Adjustment of the Mechanical Properties of Mg2Nd and Mg2Yb by Optimizing Their Microstructures

Jonas Schmidt [1,*], Irene J. Beyerlein [2], Marko Knezevic [3] and Walter Reimers [1]

1 Institute of Material Science and Technology, Technische Universität Berlin, Ernst-Reuter-Platz 1, 10587 Berlin, Germany; walter.reimers@physik.tu-berlin.de
2 Department of Mechanical Engineering, Materials Department, University of California, Santa Barbara, CA 93106, USA; beyerlein@ucsb.edu
3 Department of Mechanical Engineering, University of New Hampshire, Durham, NH 03824, USA; marko.knezevic@unh.edu
* Correspondence: jonas.schmidt@tu-berlin.de; Tel.: +49-030-314-26715

Abstract: The deformation behavior of the extruded magnesium alloys Mg2Nd and Mg2Yb was investigated at room temperature. By using in situ energy-dispersive synchrotron X-ray diffraction compression and tensile tests, accompanied by Elasto-Plastic Self-Consistent (EPSC) modeling, the differences in the active deformation systems were analyzed. Both alloying elements change and weaken the extrusion texture and form precipitates during extrusion and subsequent heat treatments relative to common Mg alloys. By varying the extrusion parameters and subsequent heat treatment, the strengths and ductility can be adjusted over a wide range while still maintaining a strength differential effect (SDE) of close to zero. Remarkably, the compressive and tensile yield strengths are similar and there is no mechanical anisotropy when comparing tensile and compressive deformation, which is desirable for industrial applications. Uncommon for Mg alloys, Mg2Nd shows a low tensile twinning activity during compression tests. We show that heat treatments promote the nucleation and growth of precipitates and increase the yield strengths isotropically up to 200 MPa. The anisotropy of the yield strength is reduced to a minimum and elongations to failure of about 0.2 are still achieved. At lower strengths, elongations to failure of up to 0.41 are reached. In the Mg2Yb alloy, adjusting the extrusion parameters enhances the rare-earth texture and reduces the grain size. Excessive deformation twinning is, however, observed, but despite this the SDE is still minimized.

Keywords: Mg-RE alloys; extrusion; mechanical properties; microstructure; in situ diffraction; crystal plasticity; deformation twinning; texture

1. Introduction

Magnesium is one of the lowest density ($\rho = 1.7$ g/cm^3) metallic structural materials. Due to its high specific strengths, it is suitable for lightweight construction applications in the electronic industry, the biomedical industry, and the sports equipment sector [1–4]. However, the poor formability at room temperature limits the processing possibilities of magnesium alloys [5,6].

The low ductility and formability is caused by the hexagonal crystal system of magnesium, which only offers primary deformation systems in the basal plane. The <a> basal slip contributes to plastic deformation at low applied stresses due to its small critical resolved shear stresses (CRSS). Together with the <a> prismatic slip system, which requires higher activation energies, deformation can only can be realized in the <a> direction. Deformation in the <c> direction is only possible with <c + a> pyramidal slip systems, which are hard to activate [7–10]. Recently published studies show that <c + a> pyramidal slip is important for high elongations of magnesium alloys [11].

Plastic deformation can also be realized by twinning. In twinning, the crystal structure is reoriented by a defined angle along a plane of symmetry [12,13]. This induces a

microscopic change in length and contributes to macroscopic deformation [14,15]. The twin systems are divided into {10.1} tension twinning (TTW-ing) and {10.2} compression twinning (CTW-ing), depending on the stress applied along the c-axis of the unit cell. TTWs are formed when applying either tension along the c-axis or compression perpendicular to it and feature an 86° rotation about a <11.0> axis [12,13,16]. TTWs usually have a low CRSS and are, therefore, more easily activated. In contrast, CTWs with a higher CRSS feature a 56° rotation about a <11.0> axis when compression stress is applied parallel to the c-axis.

Twin formation is a unidirectional deformation mechanism that depends on the orientation of the crystals and the applied stress. In both monocrystalline and polycrystalline magnesium products, the properties depend on the orientation of the crystals and are affected by the production parameters. Typically extruded AZ31-alloys show fiber textures after extrusion [17] in which the basal planes are oriented parallel to the direction of extrusion. When compressive stress is applied along the extrusion direction, the perpendicular aligned c-axes of the grains are subjected to tensile stress, preferably forming tensile twins [18]. Due to the low CRSS of tensile twins, the compressive yield strength (CYS) is much lower than the tensile yield strength (TYS) in the extrusion direction. This asymmetric mechanical behavior is described by the Strength Differential Effect (SDE) [19,20]. For practical applications of structural materials, it is desirable to have a symmetrical material behavior, equivalent to an SDE close to 0.

The texture can be modified by changing the production/extrusion parameters and alloying elements. Studies have shown that rare earth [RE] elements can have a strong influence on the recrystallization texture [17,21,22]. They alter the grain orientations and weaken the texture during hot deformation/extrusion. Depending on the resulting orientations, various deformation mechanisms are active during subsequent cold deformation. The CRSS and the contribution to the total deformation of the individual systems have an influence on the resulting macroscopic mechanical properties.

RE solutes are used in the Mg alloys of the WE-series, containing 7 to 9% RE, mainly yttrium (Y) and neodymium (Nd) [23,24]. Although the alloys are characterized by high strength, high costs make it desirable to reduce the RE content while maintaining the advantageous properties. Neodymium in particular is suitable, as it achieves good properties and strongly influences the texture [25]. Seitz et al. [26] extruded an Mg2wt.%Nd alloy and found a small asymmetry in the tension and compression.

For this study, two magnesium alloys with 2 wt.% rare earth content, Mg2Nd and Mg2Yb, were investigated with regard to their microstructure, deformation behavior, and mechanical properties. By varying the process parameters, the microstructure can be changed so that the strength and ductility can be adjusted over a wide range. In particular, a significant reduction in the SDE can be achieved.

In a first step, two casted billets of each alloy were extruded, varying the cooling conditions. The extruded bars were investigated by electron microscopy (SEM, TEM), laboratory X-ray texture measurements, and mechanical testing (compression, tension) to determine the mechanical properties, the microstructure, and their changes during deformation. To gain further insight into the different deformation behavior, a combination of in situ energy-dispersive X-ray synchrotron diffraction and simulations with the elasto-plastic self-consistent (EPSC) model was used [27]. The particular version of the model used in the present work is from [28]. These methods allow an analysis of the active deformation mechanisms as a function of load. Furthermore, the parameters of a dislocation density-based strain hardening model of the different deformation mechanisms are obtained. By adding Nd, an advantageous texture can be achieved. The texture activates similar deformation systems at the beginning of plastic preforming and, in particular, effectively suppresses the formation of tensile twins under compressive stress. The addition of Yb has a lower impact on the texture and a more pronounced dynamic recrystallization can be observed. This results in low strengths and high SDEs.

In the next step, heat treatments and variations in extrusion parameters were used to modify the microstructure and thus the mechanical properties. The grain size was reduced

while maintaining or even improving the advantageous texture. Due to the low solubility of Nd and ytterbium (Yb) in Mg, subsequent heat treatments were used to further increase the strength. In the Mg2Nd alloy, subsequent heat treatments lead to the formation of fine precipitates, generating a significant hardening effect. In the case of the Mg2Yb alloy, heat treatments for precipitation hardening are less effective. However, by adjusting the process parameters the grain size can be reduced and the texture improved as well, so that, despite differences in plastic deformation, the yield strengths in compression are almost equal to the yield strengths in tension. This resulted in high strengths and low SDEs.

2. Materials and Methods

2.1. Material, Microstructure

The extrusion billets had a nominal composition of Mg2wt.%Nd (Mg2Nd) and Mg2wt.%Yb (Mg2Yb) with a diameter of 123 mm and a length of 115 mm. They were casted at the Helmholtz-Zentrum Geesthacht (HZG). The billets were homogenized and solution annealed in the single-phase region of the phase diagram [29]. Depending on the composition and phase diagram, the temperature was 500 °C (6 h) for the Mg2Nd alloy and 450 °C (10 h) for Mg2Yb with an 8 h heating period. After the heat treatment, the billets were quenched in water. Prior to extrusion, the billets were inductively heated rapidly to extrusion temperature and then immediately extruded. The indirect extrusion process was carried out at the Technische Universität Berlin, Extrusion Research and Development Center, varying some of the extrusion parameters including billet temperature (T_B), cooling method, extrusion ratio (R), and product speed (v_P), as shown in Table 1.

Table 1. Extrusion parameters.

Alloys	Series	T_B (°C)	Cooling	R	v_P (m/min)
	A	400	Air	61:1	0.5
Mg2Nd	B	400	Water	61:1	0.5
	C	400	Water	61:1	0.25
	A	400	Air	61:1	1.3
Mg2Yb	B	400	Water	61:1	1.6
	C	300	Water	61:1	1.8

To improve the mechanical properties with regard to technological application, the extruded bars were subsequently heat-treated at different temperatures (150, 204, and 300 °C). To determine the heat treatment duration, hardness tests were performed on samples of different ageing times. Samples with the highest hardness were further selected for mechanical testing with tensile and compression tests.

For optical microscopy and grain size analyses, the as-extruded specimens were prepared by grinding and polishing and subsequent chemical polishing with a solution of 12 mL hydrochloric acid (37%), 8 mL nitric acid (65%), and 100 mL ethanol. Etching with a picric etching solution (4.2 g picric acid, 10 mL acetic acid, 10 mL H_2O, and 70 mL ethanol) revealed the grain structure. To examine precipitates in the SEM, polished samples in the as-extruded and heat-treated states were used.

Thin TEM foils were cut, mechanically polished, and electrolytically thinned by a twin-jet TenuPol 3 with a solution of 5.3 g lithiumchloride, 11.16 g magnesiumperchlorate, 500 mL methanol, and 100 mL 2-butoxy-ethanol.

HR-TEM images were recorded on a FEI Tecnai G2 20 S-TWIN TEM and a FEI Titan 80–300 Berlin Holography Special TEM (Technische Universität Berlin, Zentraleinrichtung Elektronenmikroskopie).

For energy-dispersive synchrotron in situ tests, compression specimens with a diameter of 7 mm and a length of 15 mm and tensile specimens with a diameter of 6 mm and a length of 36 mm were used.

The texture of the polished specimens in the as-extruded conditions and deformed state were measured with the laboratory X-ray diffraction method using CoKα radiation

and a 3 mm collimator. The experimental pole figures for the (10.0), (0002), (10.1), (10.2) and (11.0)-reflections were measured and the inverse pole figures were calculated from the experimental data using the MTEX software package [30].

Compression samples (D = 10 mm, l_0 = 20 mm) and tensile samples (D = 6 mm, l_0 = 36 mm) were machined from the extruded bar. Compression samples were compressed up to engineering strains of -0.01, -0.04, -0.08, -0.15, and to fracture, while tensile samples were deformed to fracture. The quasi-static tension and compression tests were carried out with a universal testing machine (MTS810) with strain rates of $2.5 \times 10^{-4}\,s^{-1}$.

For extruded magnesium alloys, the yield strength in tension (TYS) has been reported to be higher than the yield strength in compression (CYS). This difference in strength is called the strength differential effect (SDE) and can be expressed as:

$$\mathrm{SDE} \ = \ \frac{|\mathrm{CYS}| - |\mathrm{TYS}|}{|\mathrm{CYS}| + |\mathrm{TYS}|}. \tag{1}$$

2.2. In Situ Energy Dispersive Synchrotron X-Ray Diffraction

In situ energy-dispersive synchrotron X-ray diffraction experiments were carried out at the 7T-MPW-EDDI-beamline at the BESSY-II synchrotron [31]. The beamline is equipped with a superconducting 7T multipole wiggler, which provides a white beam with a usable range of about 8 to 150 keV. For the experiments, an energy range of 20 to 60 keV and the Bragg angle 2θ of 10.34° were used. The beam was limited by slit systems to $1 \times 2\,mm^2$ on the incoming and $0.1 \times 7\,mm^2$ on the detector side. The in situ compression and tensile tests were carried out with a tensile-compressive loading device designed by Fa. Walter+Bai AG, which is mounted on a 4-axes positioner to allow x-y-z translation and Ψ rotation around the axis of the beam.

In the unloaded sample state, the lattice spacings d_0^{hkil} were measured in 11 Ψ angles between 0 and 89.9° with an exposure time of 60 s. These data were used for the determination of d_0^{hkil}. During mechanical testing, the d^{hkil} were measured at several uniaxial tensile and compression steps at 0° and 89.9° to determine the elastic lattice strains ε^{hkil} in the axial and transversal direction by Equation (2) [32]:

$$\varepsilon^{hkil} = \frac{d^{hkil}}{d_0^{hkil}} - 1 \ = \ \frac{E_0^{hkil}}{E^{hkil}} - 1. \tag{2}$$

Here, d^{hkil}, d_0^{hkil}, and E^{hkil}, E_0^{hkil} are the lattice spacings and their corresponding diffraction lines at a load step and prior loading. The in situ measurements were stress controlled in the linear elastic region. After reaching the yield strength, displacement control was used.

2.3. EPSC Modeling

The elasto-plastic self-consistent (EPSC) model [27] is a polycrystal plasticity model which simulates the constitutive response of a material based on single crystal data, a hardening model, given texture, and initial grain shape and size. A recent description of the formulation used here can be found in [28,33,34].

To describe hardening, separate models are employed for slip and twinning. For slip, a dislocation density-based hardening model for the CRSS values in different crystallographic slip systems is employed [35,36]. For twinning, a model for the domain reorientation and twin expansion as well as the twin boundary effect on slip is used, as described by the composite grain model [37]. To activate twinning, we employ the finite initial fraction (FIF) assumption [7], which states that twin nucleation is accompanied by twin growth to a finite initial fraction. For the simulations here, an FIF of 0.01 is used.

The material parameters used in the model pertain to elasticity, the initial stress to activate slip, the rates of dislocation storage, and the critical stress for twin growth. These are listed in Table 3. For the first of these, we used single-crystal elastic constants for Mg, which are C_{11} = 59.5 GPa, C_{12} = 26.1 GPa, C_{13} = 21.8 GPa, C_{33} = 65.6 GPa, and C_{44} = 16.3 GPa for both alloys. The remaining parameters were identified iteratively and specifically for each alloy until the simulation results matched all the experimental results. The simulation results enable da direct comparison with the synchrotron X-ray diffraction measurements from the compression and tensile tests. The average stress–strain response, the texture evolution, and the elastic lattice strains allow to check the EPSC predictions by the experimental diffraction data. The EPSC simulation further gives information on the active deformation modes and their CRSS as a function of the strain. For the final simulation, a grain set of 10,000 grains, which represent the as-extruded texture, was used.

3. Results

3.1. Microstructure

The microstructure of the as-extruded material is presented in Figure 1 via optical micrographs to show the grain structure and inverse pole figures to show the texture. The microstructures of all three series are dominated by globular recrystallized grains. The average grain size of the Mg2Nd alloy decreases from 13 ± 1 μm for the air-cooled A-series to 7 ± 1 μm for the water-quenched B-series. This is due to hindered grain growth after the dynamic recrystallization caused by the rapid drop in temperature. An additional decrease to an average grain size of 3 ± 1 μm for the C-series was achieved by reducing the extrusion speed. The Mg2Yb alloy shows an average grain size of 49 ± 4 μm for the air-cooled A-series and 26 ± 2 μm for the water-quenched B-series. Extrusion at a reduced temperature decreases the grain size of the C-series to 8 ± 2 μm. In the slower extruded C-series of the Mg2Nd alloy and both water-quenched series of the Mg2Yb alloy, elongated grains that are not fully recrystallized are occasionally found in the longitudinal sections (Figure 1h,n,q).

The X-ray diffraction texture measurements reveal pronounced RE-fiber-textures with overall low maximum intensities (Figure 1). The texture of the A-series of the Mg2Nd alloys has a maximum at the <11.2>pole and the B-series shows additional intensity between the <10.2> and <10.1>pole. The C-series has its maximum at the <10.0> pole with additional intensities at the <10.1> and<11.2> pole. The A- and C-series of the Mg2Yb alloys show a very weak extrusion texture with of maximum of just 1.3 multiples of random distribution (mrd) and 1.5 mrd, respectively, and intensities at the <10.2> and <11.2> pole. The B-series, in contrast, shows the highest observed intensity of 2.3 mrd at the <10.0> pole. The texture of the C-series is similar to the A-series, with an additional intensity at the <10.0> pole.
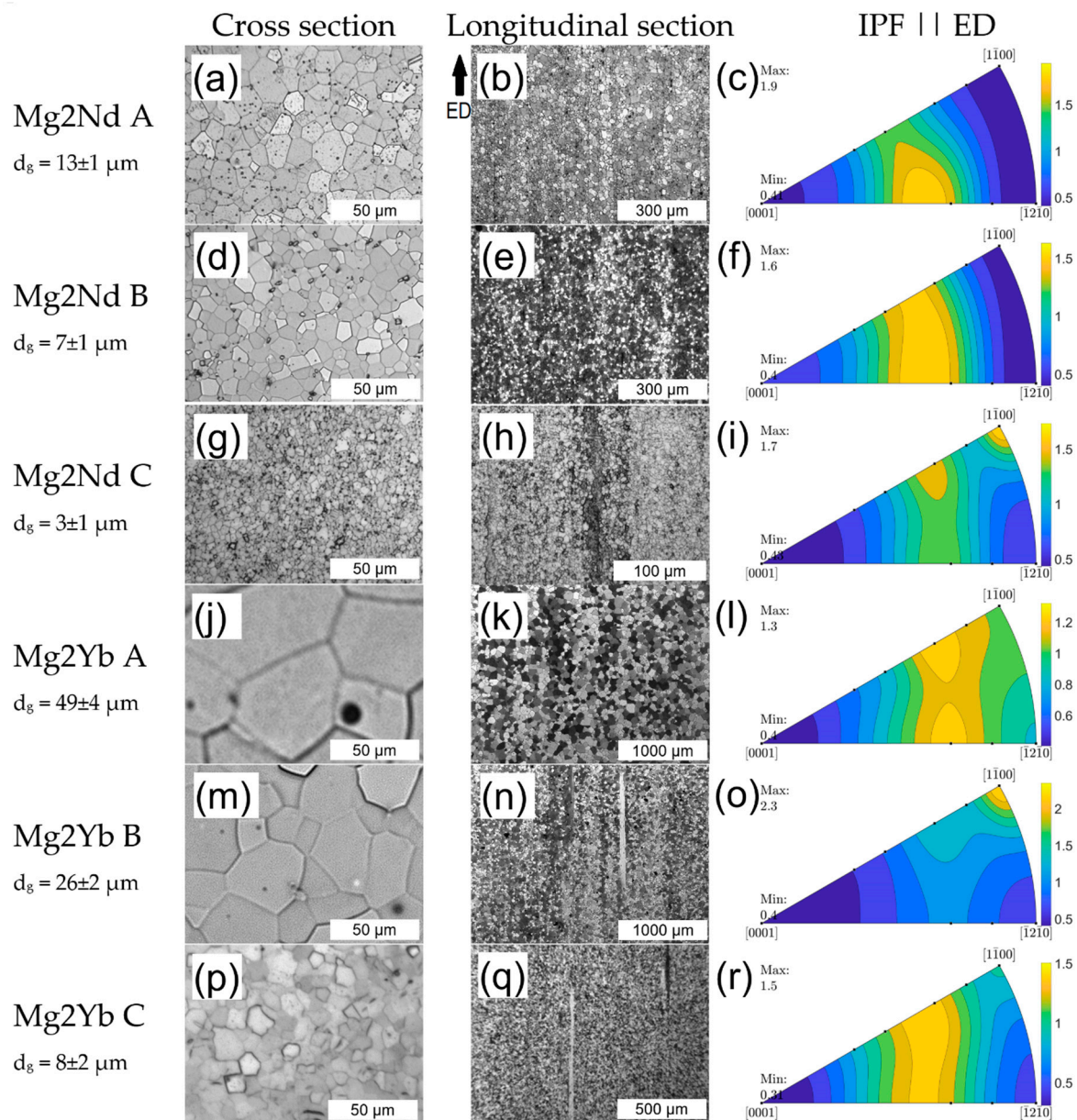
Figure 1. Cross section, longitudinal section, and inverse polfigures in the extrusion direction (ED) of the Mg2Nd alloy (**a–c**) A-series, (**d–f**) B-series, (**g–i**) C-series, and of the Mg2Yb alloy (**j–l**) A-series, (**m–o**) B-series, (**p–r**) C-series.

3.1.1. Mg2Nd

All series of the Mg2Nd alloy show coarse precipitates in different shapes and diameters up to 4 μm. These precipitates are randomly distributed in the grains. In the slower-cooled A-series, additional precipitates can be seen on the grain boundaries (Figure 2a). The area fraction of the precipitates was determined to approx. 3.2% for the A- and B-series and 3.5% for the C-series. Due to the high number of precipitates, analyses of the solution content of Nd in the Mg-matrix were carried out using a high-resolution electron probe micro-analyzer (EPMA). These showed that a Nd concentration of 1.6 wt.% was present in the matrix. Further measurements show that these are stable Nd-rich β_e (Mg41Nd5) precipitates [38]. Heat treatments at 150 °C and 204 °C promote the formation of coherent Guinier–Preston zones and β'' precipitates with diameters of 10 to 20 nm (Figure 2b) [29,38,39]. Heat treatments at higher temperatures produce stable β_e-precipitates that either do not lead to precipitation hardening or, even worse, reduce the strength. These samples were, therefore, not investigated further.
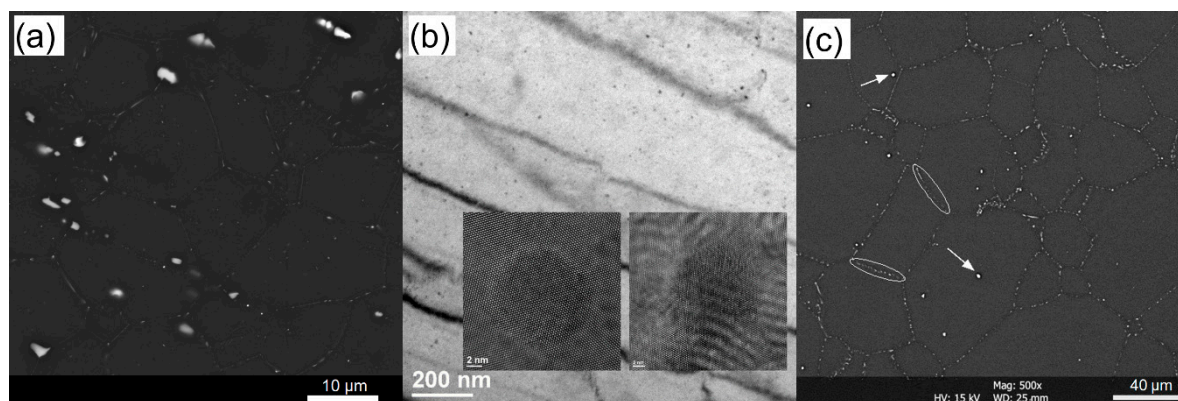
Figure 2. (**a**) SEM Mg2Nd A-series, (**b**) TEM images of precipitates in the heat-treated (150 °C, 7 h) Mg2Nd B-series, <0002> zone axis, (**c**) SEM Mg2Yb A-series.

3.1.2. Mg2Yb

In the water-quenched B and C series, only the larger precipitates with diameters of 1 to 2 μm are found in the as-extruded state. They are located within the grains and are homogeneously distributed. In samples of the A series, the same precipitates are found within the grains. In addition, predominantly smaller precipitates (Ø~0.5 to 1 μm) are observed at the grain boundaries (Figure 2c). These precipitates are the β'-phase (Mg$_2$Yb) precipitates [40], and formed after extrusion during slow cooling. Heat treatments at 150 °C have little effect on the microstructure and mechanical properties of the Mg2Yb alloy. In contrast, an increase in the phase fraction of the β' precipitates can be observed after a heat treatment for 15 min at 300 °C. No changes in grain size and texture were observed during all heat treatments of the Mg2Nd and Mg2Yb alloys.

3.2. Mechanical Properties

The yield strengths (CYS, TYS) and elongations to failure (ε_{fc}, ε_{ft}), as determined from the stress–strain curves, are summarized in Table 2. For the Mg2Nd alloy, the flow curves of the A-series look similar in compression (Figure 3a) and tension (Figure 3b), and achieve elongations to failure above 0.32. We find that the B-series shows similar behavior (Supplementary Materials Figure S3). In contrast, the shape of the flow curves of the C-series differ between the compression and tensile tests (Figure S3). The air-cooled A-series yields at −105 and 107 MPa in the uniaxial compression and tensile tests, respectively, resulting in nearly zero SDE (Table 2). Reducing the grain size to 7 μm by adjusting the cooling method (B-series) after extrusion increased the CYS and TYS to −125 and 122 MPa, respectively. In the case of the C-series alloy, the associated additional grain size reduction to 3 μm, by the slower extrusion rate, increased the CYS and TYS further to −176 and 175 MPa, resulting in an SDE of 0. However, in this case the flow curve of the compression test exhibits a sigmoidal shape (Figure S3), which is a well-known signature of tension twinning [18]. Still, the increased activity of TTW-ing significantly reduces the elongation to failure (ductility) in the compression test. The tensile test had similarly good values, just as with the A- and B-series.

Table 2. Mechanical properties of the investigated alloys (the error of compressive yield strength (CYS) and tensile yield strength (TYS) is below 5 MPa, the error of ε_{fc} and ε_{ft} is below 0.02).

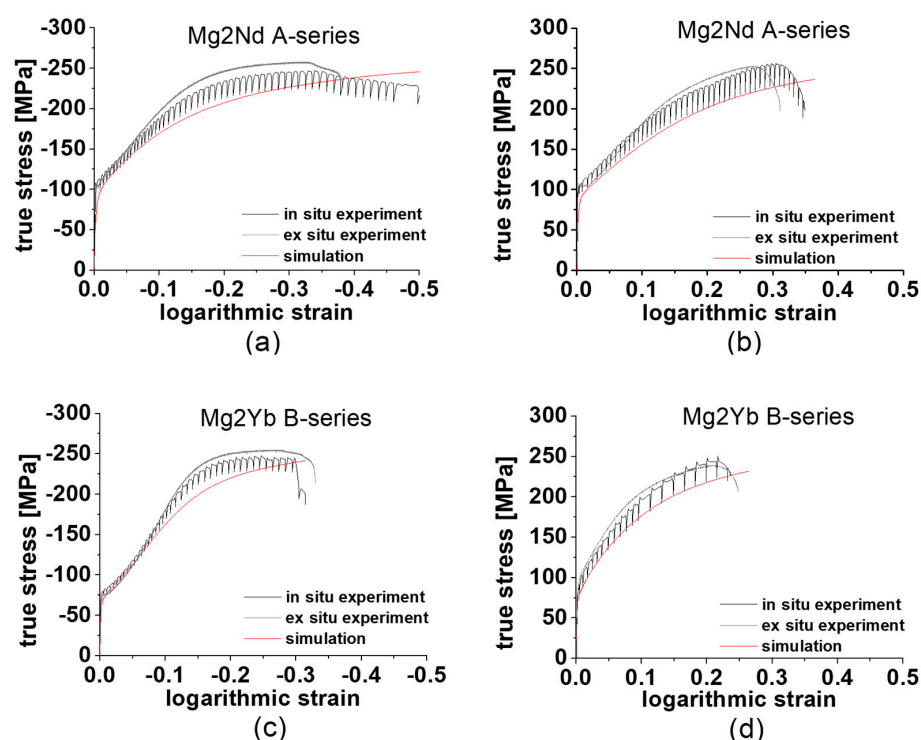| Alloy	Series	Heat Treatment	CYS (MPa)	ε_{fc} (-)	TYS (MPa)	ε_{ft} (-)	SDE
	A	-	−105	−0.32	107	0.36	−0.02
	A + HT	150 °C, 6 h	−123	−0.24	129	0.20	−0.05
	B	-	−125	−0.29	122	0.41	0.02
Mg2Nd	B + HT	150 °C, 7 h	−160	−0.24	133	0.17	0.18
	C	-	−176	−0.22	175	0.34	0.01
	C + HT	150 °C, 7 h	−197	−0.18	203	0.34	−0.03
	C + HT	204 °C, 3 h	−191	−0.2	197	0.33	−0.03
	A	-	−58	−0.3	89	0.3	−0.42
	A + HT	300 °C, 15 min	−65	−0.29	104	0.21	−0.47
Mg2Yb	B	-	−77	−0.22	100	0.32	−0.26
	B + HT	300 °C, 15 min	−83	−0.23	110	0.25	−0.28
	C	-	−111	−0.22	115	0.32	−0.04

Figure 3. Comparison of the flow curves from the in situ experiment, ex situ experiment and the simulation of the Mg2Nd A-series (**a**) compression and (**b**) tensile tests and the Mg2Yb B-series (**c**) compression and (**d**) tensile tests.

The Mg2Yb alloy is significantly more anisotropic in its plastic deformation and mechanical properties than the Mg2Nd alloy, especially in the B-series. The flow curves of the compression tests (Figure 3c and Figure S3) show a strong sigmoidal shape and the CYS are significantly lower than the TYS. This leads to SDEs of high magnitude (Table 2). Nevertheless, a strong influence of the grain size can be observed in both the CYS and TYS. As grain size decreases, the yield strengths increase and this effect is more pronounced in compression than in tension. Therefore, the C-series ultimately achieves a low SDE of −0.04.

Next, we heat-treated the series of the Mg2Nd alloys at 150 °C. We find that heat treating increases the TYS of the A-series slightly more than the CYS, leading to a larger SDE than without heat treatment. The yield strengths become similar to those of the B-series in the as-extruded state. In the case of the B-series, heat treating causes the CYS and TYS to increase asymmetrically, resulting in a strongly increased SDE. The strength of the

C-series can be increased in a similar way as that seen in the A-series. A 3 h heat treatment at 204 °C leads to a CYS and a TYS of -191 and 195 MPa (SDE = −0.03) and a 7 h heat treatment at 150 °C to −197 and 203 MPa (SDE = −0.03), respectively. While the ductility of the A series decreases significantly, the ductility of the heat-treated C-samples remains unchanged in the tensile tests. However, it decreases slightly in the compression tests.

Asymmetric precipitation hardening is even more pronounced in the Mg2Yb alloy. For both the A- and B-series, the TYS increases more than the CYS. Therefore, an increase in the SDE can be observed in both cases. While the ductility during compression deformation remains nearly the same after heat treatment, it decreases significantly during tensile deformation.

3.3. Deformed Microstructure

In order to investigate the development of the microstructure during deformation, compression tests were stopped at certain deformation steps. Figure 4 shows the grain structure and texture for the Mg2Nd A-series and Mg2Yb B-series for some of these intermediate strain levels (the microstructure and textures for the other series and at other strain levels can be found in Figures S4 and S5).
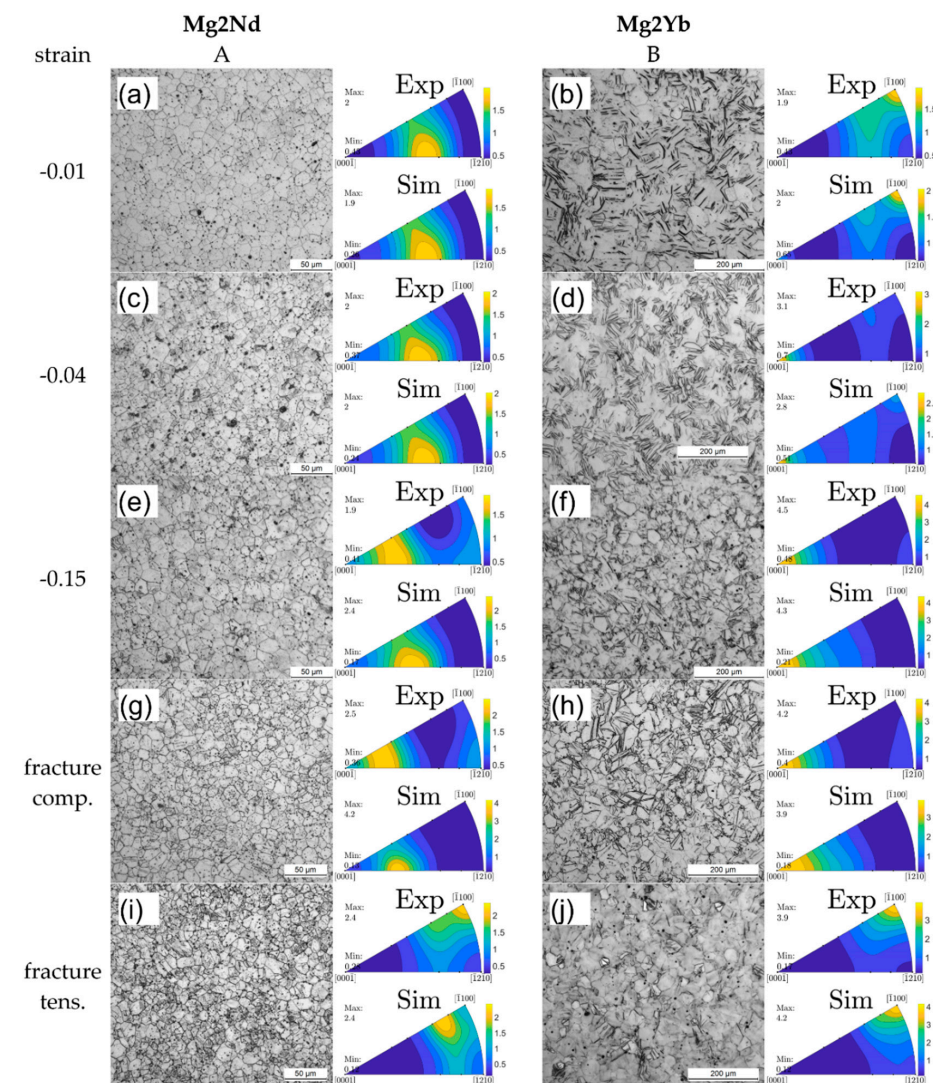

Figure 4. Cross sections and comparison of the measured and simulated texture at (**a**,**b**)−0.01, (**c**,**d**)−0.04, (**e**,**f**)−0.15 strain and elongation to failure in (**g**,**h**) compression and (**i**,**j**) tension for the Mg2Nd A-series and the Mg2Yb B-series, respectively.

3.3.1. Mg2Nd

No twins are observed in the optical micrographs of the A- and B-series of the Mg2Nd alloy. While the flow curves of the Mg2Nd alloy show a similar shape, there is a clear difference in the texture evolution between the compression and tensile tests (Figure 4g,i). The inverse pole figures show a continuous shift in texture during deformation. During compression, the maximum intensity is close to the <11.2>-pole in as-extruded state, gradually shifting towards the <0002>-basal pole with increasing deformation (Figure 4a,c,e,g). During tensile testing, however, the initial <11.2>-texture with low maximum intensities changes to a sharp <10.0>-texture (Figure 4i) with increased maxima of 3.9 and 4.4 mrd for the A- and B-series, respectively (B-series shown in Figure S4).

3.3.2. Mg2Yb

On the contrary, the excessive twinning of the Mg2Yb alloy is observed in the compressive deformation of the A- and B-series. For as little as −0.01 strain, thin twin lamellae can be observed in the optical micrographs (Figure 4b). However, these fine twins have no effect on the texture. With increasing the strain to −0.04, the area fraction of the twinned grains increases and the existing twin lamellae widen. Together the resulting rise in twin activity leads to a noticeable change in texture towards a <0002>-basal texture (Figure 4d). Specifically, due the formation and growth of twins, the maximum intensity at the <0002>-pole increases, while the initial texture slowly depletes. The intensity at the <10.0>-pole decreases both in the A- and B-series and disappears at −0.04 strain. While the <10.1> and <11.2>-texture components from the A-series can still be recognized, they too disappear at −0.08 and a strong <0002>-basal texture remains (Figure S5 and Figure 4f). With increasing deformation, the maximum intensity at the <0002>-pole further increases, an increase that is more pronounced in the B-series than in the A-series.

3.4. EPSC Simulation

To understand the deformation behavior of the investigated alloy, in situ experiments were performed. Table 3 shows the parameters used for the hardening models in the EPSC simulation. With these parameters, a good agreement was obtained between the simulated and the experimental data in terms of flow curves (Figure 3 and Figure S3) and texture evolution (Figure 4 and Figure S2). As validation, we find that the model is capable of calculating the elastic lattice strains of different crystallographic planes. The calculated elastic lattice strains are compared with those determined experimentally in the in situ tests in Figure 5, Figure S4, and Figure S5 and also show good agreement. As a result of the simulation, further insights into the deformation behavior and the activities of the deformation systems (Figure 6, Figure S6, and Figure S8), as well as their CRSS (Figure 7, Figure S7, and Figure S9), during the deformation process are gained.

Table 3. Hardening parameters for slip and twin systems.

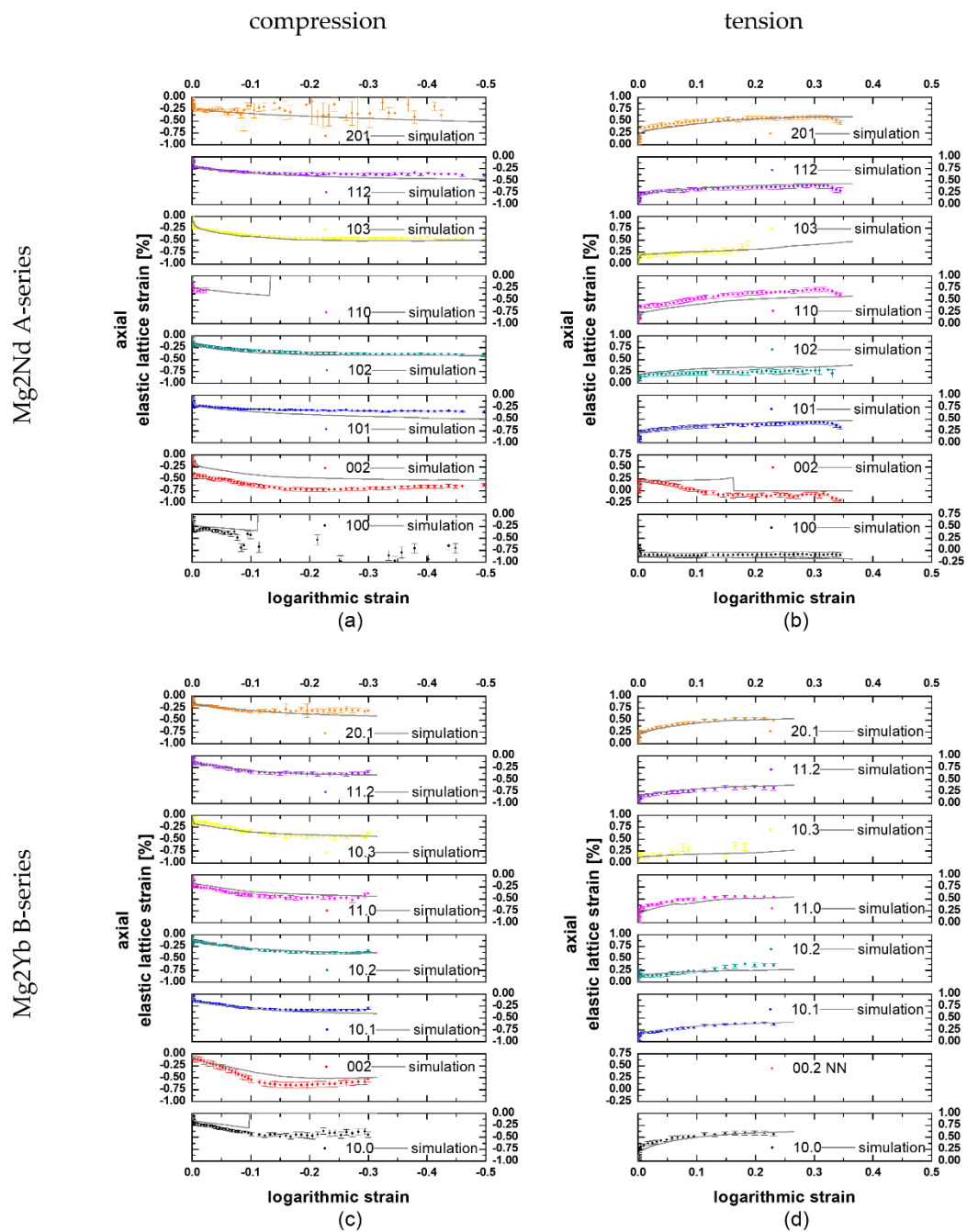| Parameter	Mg2Nd (c/a = 1.623)				Mg2Yb (c/a = 1.626)			
	Prismatic	Basal	Pyramidal	TTW	Prismatic	Basal	Pyramidal	TTW
$\tau_{0,f}^s / \tau_0^t$ **(Mpa)**	39	11	60	18	21	1	67	2
k_1^s **(m^{-1})**	2.2×10^8	6.0×10^7	4.5×10^9	-	4.0×10^8	3.0×10^7	5.5×10^9	-
D^s **(MPa)**	4.5×10^3	3.0×10^3	3.5×10^3	-	4.0×10^3	4.0×10^3	4.0×10^3	-
g^s	7.2×10^{-3}	4.3×10^{-3}	7.3×10^{-3}	-	6.5×10^{-3}	4.8×10^{-3}	7.2×10^{-3}	-
H^s, H^t	70	90	30	110	190	150	40	110
C^{st}	50	50	400	-	50	50	400	-

Figure 5. Comparison of the experimentally measured and simulated axial elastic lattice strains of the Mg2Nd A-series during (**a**) compression and (**b**) tensile tests and the Mg2Yb B-series during (**c**) compression and (**d**) tensile tests.
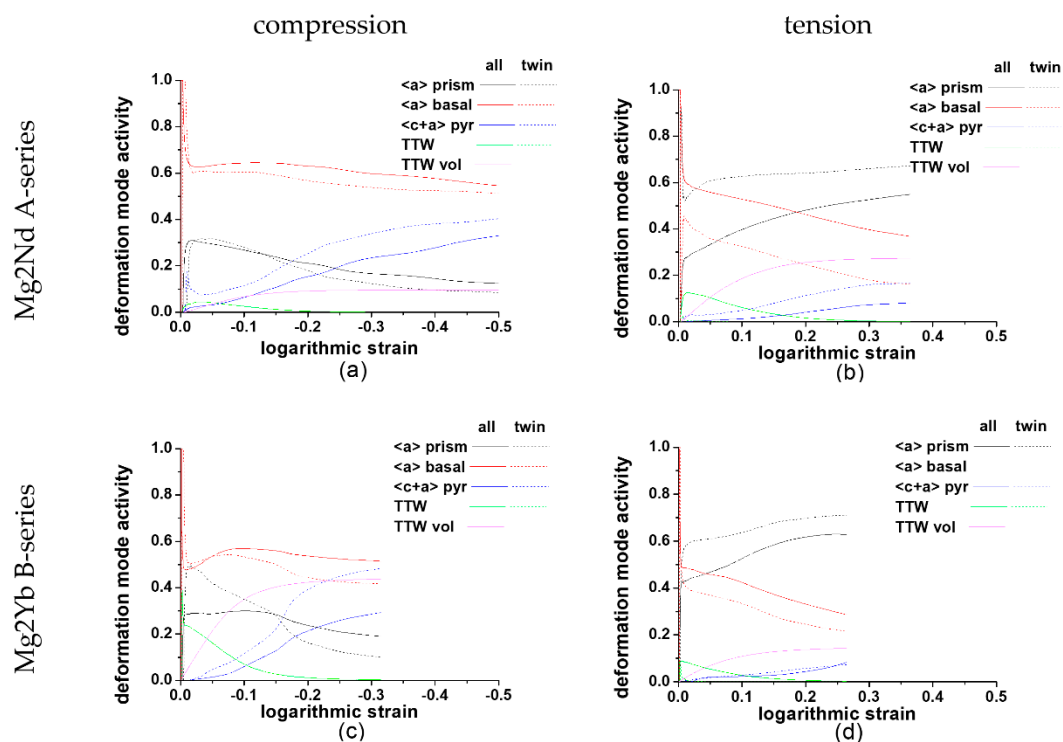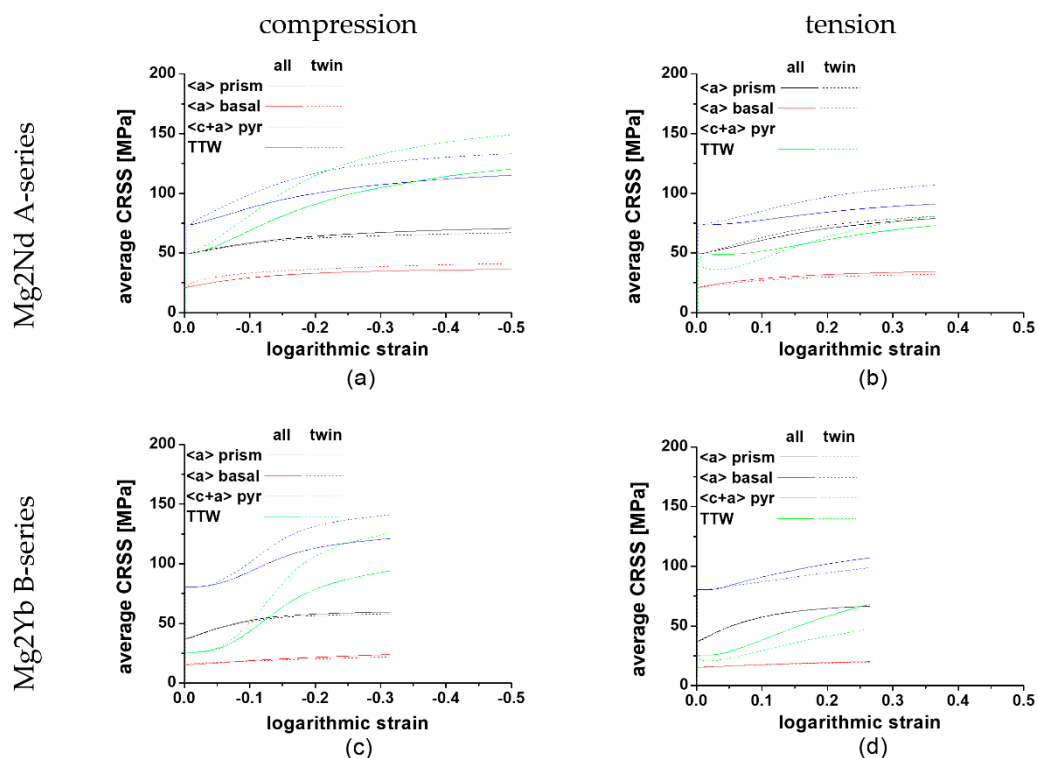
Figure 6. Deformation mode activity as a function of strain of the Mg2Nd A-series during (**a**) compression and (**b**) tensile tests and the Mg2Yb B-series during (**c**) compression and (**d**) tensile tests.

Figure 7. Critical resolved shear stresses (CRSS) of the different deformation systems as a function of strain of the Mg2Nd A-series during (**a**) compression and (**b**) tensile tests and the Mg2Yb B-series during (**c**) compression and (**d**) tensile tests.

3.4.1. Flow Curves

In the mechanical testing, the strains were applied step by step, and at each step EDS-XRD measurements were carried out. During the data acquisition steps, the material rapidly relaxed, leading to a reduced stress. The stress measurement is recorded in the relaxed state for most of the time. The simulated flow curves were matched to the experimental flow curves from the in situ tests at these reduced stresses. It should be noted that an elongated yield point (Lüders strain) was observed in the in situ tensile tests of the Mg2Nd alloy (Figure 3). However, this region was not used in the simulation model, since it does not take into account localized plastic deformation.

3.4.2. Elastic Lattice Strains

The elastic strains were calculated from the data of the in situ compression and tensile tests. These provide further information on the deformation behavior. Figure 6; Figure 7 show the evolution of the elastic lattice strains for the A- and B-series of the Mg2Nd and Mg2Yb alloys in axial direction of the (10.0), (0002), (10.1), (10.2), (11.0), (10.3), (11.2), and (20.1) reflections during the compression and tensile tests.

During deformation, grains with (10.1), (10.2), (10.3), and (11.2) orientations possess high Schmid Factors (SF) for <a> basal slip, making it the most likely active slip system in these grains. Grains with (10.0), (11.0), and (20.1) orientations have a high SF for <a> prismatic slip. Grains oriented in (0002) require <c> axis deformation to accommodate the applied load. They cannot deform by either <a> basal or <a> prismatic slip since the slip direction is perpendicular to the loading direction, and this results in an SF of zero for these <a> slip modes. Consequently, <c + a> pyramidal slip is the only possible slip system. Another mechanism accommodating <c>-axis deformation is mechanical TTW-ing. Since TTW-ing is a unidirectional deformation system accommodating only <c>-axis extension and not compression, the behavior of the alloy in tension and compression tests differs. During compression (10.0) and (11.0) -oriented grains possess a high SF for TTW-ing, whereas in tensile tests (0002) grains have a high SF for TTW-ing.

Mg2Nd

For both compression and tensile tests, the grains associated with <a> basal slip ((10.1), (10.2), (10.3), and (11.2)) show the lowest initial elastic lattice strains in the axial direction. With increasing deformation, only a small increase in elastic lattice strains can be observed. Grains associated with <a> prismatic slip ((10.0), (11.0), and (20.1)) exhibit higher initial elastic lattice strains, which increase with further deformation. During compression, the intensity of these reflections decreases and gradually disappears, leading to greater inaccuracies of the calculated elastic lattice strains. Eventually the (10.0), (11.0), and (20.1) reflections disappear, so the elastic lattice strains can no longer be determined. Equivalent observations were made for the (0002) grains during tensile deformation. During compression, the grains oriented in (0002) initially show the highest elastic lattice strains, which increase the most during plastic deformation. They reach their maximum at a strain of -0.15 and remain almost constant thereafter.

Mg2Yb

For the A- and B-series of the Mg2Yb alloy, a similar evolution of the elastic lattice strains is observed. However, during compression grains associated with <a> prismatic slip ((10.0), (11.0), and (20.1)) can be analyzed at all times. Yet, similar to the Mg2Nd alloy, increasing inaccuracies can be observed with increasing deformation. Small initial elastic lattice strains in these orientations associated with <a> basal slip ((10.1), (10.2), (10.3), and (11.2)) indicate a low CRSS to activate plastic deformation, or, vice versa, higher elastic lattice strains indicate a higher CRSS. In addition, the increase in the elastic lattice strains can be associated with the work hardening of the active slip system. The EPSC model can quantify these qualitative predictions and calculate the evolution of the CRSS of the different deformation systems and their contribution to the total deformation.

3.4.3. Activities and CRSS of Deformation Systems

Mg2Nd

Compression

The deformation during uniaxial compression is mainly carried by <a> basal slip with a constant contribution of approximately 0.6 (Figure 6a) and little work hardening. This can be seen in the low increase in the CRSS (Figure 7a). The maximum SF of <a> basal slip is not affected by the continuous texture change and remains at a high value of 0.49. Initially, the <a> prismatic slip system is the second most active, but its activity decreases continuously. It shows more hardening (increase in the CRSS) than the <a> basal slip system. TTW-ing only has a minor role at the beginning. As previously seen in Figure 4, there are only few twinned grains at a strain of −0.08. After a total strain of −0.1 to −0.15, the activity of TTW-ing is negligible. As the activity of <a> prismatic slip and TTW-ing decreases, the <c + a> pyramidal slip system becomes more important at higher strains. The elastic lattice strain of the (0002) plane increases continuously up to a deformation of approximately −0.15 true strain. Afterwards, they remain at a constant level. This means that up to this strain, the deformation of the grains in (0002) or c-direction is mainly carried out elastically. Subsequently, an increase in the deformation activity of the <c+a> pyramidal slip can be observed, accompanied by a significant increase in the CRSS.

Tension

As with compression deformation, the <a> basal slip system is the most important deformation system in the early stages of straining. However, the contribution decreases continuously from 0.55 to 0.4, while the share of the <a> prismatic slip system increases and exceeds the share of the <a> basal slip system at a total strain of about 0.15 (Figure 6b). The CRSS of the <a> prismatic slip system behaves in the same way as the <c + a> pyramidal slip system under compressive stress. The increased activity of the <a> prismatic slip system is accompanied by a much stronger increase in CRSS (Figure 7b). Compared to the compression test too, an increased activity of TTW-ing is observed in the tensile test, thus leading to a higher final total volume of twinned grains.

Mg2Yb

Compression

As suggested in the texture evolution, TTW-ing contributes to deformation at small strains. The B-series alloys achieve a higher volume fraction of TTW than the A-series alloys. The B-series also has a higher proportion of TTW volume fraction than the A-series. This can be attributed to the more pronounced <10.0> texture component. For the slip systems, the <a> basal slip is the most active. Its volume fraction increases up to 0.6 with decreasing TTW-ing (Figure 6c). The portion of <a> prismatic slip decreases slightly with increasing deformation. In the range of ×0.1 to −0.15 deformation an increase in <c + a> pyramidal slip can be observed. The twinned grains, which are oriented in (0002), can now only deform further by <c + a> pyramidal slip. The CRSS of the <c + a> pyramidal slip increases highly for the twinned grains (Figure 7c). In contrast, the CRSS of the <a> basal and <a> prismatic slip shows a weaker increase. The CRSS of the TTW-ing increases more than the CRSS of the slip systems.

Tension

In the tensile tests, <a> prismatic slip is the dominant deformation system (Figure 6d). The share of the total deformation increases with increasing strain, whereas the contribution of the <a> basal slip continuously decreases. Since there are only a few grains oriented in (0002) in the original texture, a low activity of TTW-ing can only be observed at the beginning. After completion, there are no more grains with this orientation. Therefore, the proportion of <c + a> pyramidal slip is also low. Just as in compression tests, the CRSS of TTW-ing increases strongly as soon as all favorably oriented grains are twinned (Figure 7d).

4. Discussion

4.1. Strength

Plastic deformation can be carried out by different deformation systems such as crystallographic slip and mechanical twinning. A deformation system is activated if the shear stress τ exceeds the CRSS of the respective deformation system. The magnitude of the shear stress depends on the orientation of the planes with respect to the direction of loading. Thus, the texture has a significant influence on which deformation systems can be activated to which extent. The activity of the respective deformation systems and their CRSS, in turn, have a significant influence on the mechanical properties. Additionally, the CRSS of polycrystalline materials depends on the grain size.

From the yield strengths displayed in Table 2, the following dependencies (Table 4), regarding grain size can be calculated using the Hall–Petch relationship:

$$YS = \sigma_0 \frac{K}{\sqrt{d}}. \tag{3}$$

Table 4. Calculated Hall–Petch parameters.

Alloy	Mg2Nd		Mg2Yb	
HP Parameter	**CYS**	**TYS**	**CYS**	**TYS**
K (MPa μm$^{0.5}$)	239 ± 14	232 ± 29	243 ± 28	116 ± 22
σ_0 (MPa)	-37 ± 6	39 ± 12	-25 ± 7	74 ± 6

As seen in Table 4, the Hall–Petch parameters for the Mg2Nd alloy show similar values for compression and tension, with both having large values for the K-factor. This indicates the direct dependence on the grain size. The initial texture of the A- and B-series activates similar slip systems at the beginning of the compression and tensile deformation. As a result, the CYS and TYS are also similar, resulting in a low SDE. In contrast, the texture of the C-series is altered and grains elongated in ED are observed (Figure 1h). This favors TTW-ing, as seen in the flow curves (Figure S3) [16,41]. However, this does not lead to a reduced CYS (-176 MPa) compared to the TYS (175 MPa). This is due to the strong dependence of the CRSS$_{ttw}$ on grain size (Table 5), maintaining an SDE of 0.

Table 5. Initial critical resolved shear stresses (CRSS) for the different slip and twinning modes.

Alloy	Series	GS (μm)	CRSS$_{ba}$	CRSS$_{pr}$	CRSS$_{py}$	CRSS$_{ttw}$	CRSS Ratio ba:pr:py:ttw
Mg2Nd	A	13	20.7	49.2	73.4	49.4	1: 2.4: 3.6: 2.4
	B	7	23.2	51.1	74.7	61.6	1: 2.2: 3.2: 2.7
Mg2Yb	A	49	12.7	34.4	79.5	19.7	1: 2.7: 6.3: 1.6
	B	26	15.0	37.3	80.4	25.6	1: 2.5: 5.4: 1.7

On the other hand, the Hall–Petch parameters of the Mg2Yb alloy for CYS and TYS are different. For the CYS, a stronger dependence on grain size can be observed than for the TYS. This can be explained by the fact that during compression tests of the Mg2Yb alloy, a high activity of TTW-ing and <a> basal slip carry the plastic deformation initially (Figure 7b). The CRSS values for TTW-ing and <a> basal slip have a strong dependence on grain size (Table 5). In contrast, the <a> prismatic slip system is more active during tensile deformation. With a decreasing grain size from 49 μm to 26 μm for the A- and B-series, the CRSS of TTW-ing and <a> basal slip increases by 30% and 18%, respectively. On the other hand, the CRSS of <a> prismatic and <c + a> pyramidal slip only increases by 8% and 1%, respectively. The sigmoidal shape of the flow curve in the compression test (Figure S3) indicates that TTW-ing is still an important deformation system in the C-series.

Due to further reductions in grain size, however, the CRSS$_{ttw}$ has most likely continued to increase. As a result, the CYS increases relatively more than the TYS, which was also observed in the mechanical data (Table 2). According to this, the SDE was reduced from -0.42 for the A-series to -0.04 for the C-series. Subsequent heat treatments at 300 °C further increased the yield strengths of the A- and B-series. Since the CYS increases less than the TYS, it can be assumed that the precipitates have a stronger hardening effect on the initially dominant <a> basal and <a> prismatic slip systems in tensile deformation than on the TTW-ing, which occurs during compression.

4.2. Plastic Deformation

Under compressive load, the slip plane normal of an active slip system rotates in the direction of the load. During tensile deformation, the crystal also rotates continuously in such a way that the slip direction approaches the loading direction.

4.2.1. Mg2Nd

Since the texture shifts continuously toward the <0002> basal pole, it can be associated with <a> basal slip. Figure 8 shows that the initial texture (Figure 1) also exhibits high Schmid Factors for the <a> basal slip system, making it even more favorable for activation. The slow rotation of the grains toward the <0002> orientation results in a smaller SF for <a> prismatic slip and a larger SF for <c + a> pyramidal slip. In simulation, a continuous decrease in the activity of the <a> prismatic slip is observed with increasing deformation and texture shift, while the activity of the <c + a> pyramidal slip increases (Figure 6a). During tensile deformation, the texture shifts toward the <10.0> pole; therefore, <a> slip systems must be responsible for this as well (Figure 4i). Initially, the <a> basal slip system has a higher SF than the <a> prismatic slip system. Yet, at higher strains, this changes and <a> prismatic slip becomes the favored deformation system, resulting in an increase in the deformation mode activity. The increased activity of <c + a> pyramidal slip in compression tests and <a> prismatic slip in tensile test leads to higher dislocation densities and work hardening. This can be observed in the different increases in their CRSS (Figure 7b). The CRSS of the <c + a> pyramidal slip system shows the highest increase during compression, while <a> prismatic slip hardens the most under tension.
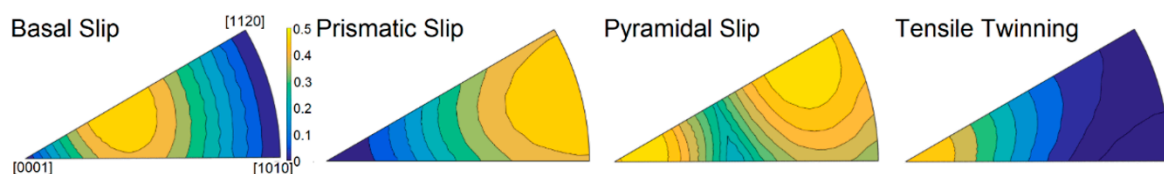

Figure 8. Theoretical calculated Schmid Factors as a function of grain orientation for uniaxial tension, displayed as inverse polfigures.

4.2.2. Mg2Yb

Compared to the continuous texture shift in the compression and tensile tests of the Mg2Nd series, the compression tests of the Mg2Yb series show an abrupt texture change (Figure 4d). This is related to the formation of TTWs. After approx. -0.1 deformation, the TTW-ing is mostly completed. The twinned grains initially also deform with <a> slip systems, but as the deformation increases <c + a> pyramidal slip becomes the dominant deformation system. This leads to grain rotation in the direction of the <11.3> slip direction, so that the <0002> texture becomes less pronounced and the intensity is spread further around the basal pole. In tensile tests, a similar behavior to the series of the Mg2Nd alloy is observed. Yet, since the initial texture is different and <a> prismatic slip is favored, a higher activity can be observed at the beginning of the deformation. As a result, it becomes the dominant deformation system even at lower strains compared to the Mg2Nd alloy series.

4.3. Ductility

Mg and most Mg alloys have a low ductility at room temperature. This is mainly due to the hexagonal crystal structure, which bears only a small number of easily activated slip systems. At room temperature, the <a> basal slip system usually has significantly lower CRSS values than the non-basal slip systems, which is why deformation at low temperatures is mainly realized by <a> basal slip. The <a> basal slip system, however, has only two independent slip systems and thus does not meet the von Mises criterion of deformation compatibility, which states that at least five independent slip systems are required for uniform plastic deformation.

By modifying the texture, the deformation behavior and thus the mechanical properties can be improved. Additions of rare earth elements showed texture changes that may have had a positive effect on the deformation behavior and especially on the ductility at low temperatures. Investigations by Stanford et al. [21] showed that the extrusion product of a binary Mg-Gd alloy (1.5wt.%Gd) with modified Mg extrusion texture achieves twice the elongation to failure of an extrusion product of pure magnesium with a comparable grain size and typical Mg extrusion texture (<10.0>/<11.0> double fiber texture). Due to the comparable grain size, the increase in ductility could be directly attributed to the texture modification.

These findings and the presented microstructure and texture suggest good ductility and good mechanical properties of the extruded products. In these modified textures, a significantly higher number of grains shows a favorable orientation for the activation of the <a> basal slip system. At the same time, fewer grains are favorably oriented for the activation of the TTW system, which further can reduce the asymmetry of the tensile and compressive yield strength (SDE). The higher activity of the basal slip system results in a higher ductility at room temperature.

The A- and B-series of the Mg2Nd alloy show <11.2> textures (Figure 1). This means that the c-axis of the majority of grains is tilted by 45–50° to the extrusion direction. The grains are in a favorable orientation for the activation of the <a> basal slip system. The higher activity of the <a> basal slip system results in a higher ductility at room temperature. Meanwhile the C-series has an additional <10.0> texture component and therefore increased TTW activity in compression tests, as seen in the flow curves (Figure S3). This leads to reduced elongation to failure in compression tests, compared to the A- and B-series, while the elongation to failure in tensile tests reaches similar values (Table 2). In all cases, heat treatments for precipitation hardening result in reduced elongation at failure for the Mg2Nd alloy. Considering this, the grain size reduction by adapting the cooling conditions, as seen in the B-series, is preferable to a subsequent heat treatment of the A-series. Similar yield strengths can be achieved by both methods. However, the ductility of the B-series is better than that of the A-series, suggesting that the additional process step of heat treatment is not necessary.

In contrast, the A- and B-series of Mg2Yb alloy have different textures. The A-series has an extraordinarily weak texture with a maximum intensity of just 1.3 mrd, nearly completely random, with intensities at <11.2> and <10.1> poles, while the B-series has a distinct <10.0> texture. This results in a difference in the ductility. Despite the unfavorable texture, the A-series deformed at lot due to TTW-ing in the compression test due to the large grain size (as explained in 4.1). The TTW are reoriented by 89°, so that they are not exactly oriented in <0002> but slightly tilted, depending on the initial orientation. This results in a wider spread compared to the B-series, which has a strong <0002> texture with a higher intensity (Figure S5). The TTW in the A-series can deform by <a> basal and <a> prismatic slip due to the tilt. While the majority of the twinned grains in the B-series are unfavorably oriented for the <a> basal slip system, the activity of the <a> basal slip system is, therefore, correspondingly low. As a result, the twinned grains deform primarily due to <c+a> pyramidal slip (Figure 6c). This leads to limited ductility and crack initiation due to stress concentrations.

5. Conclusions

Three approaches were used to modify the microstructure to adjust the mechanical properties and reduce the asymmetric yield behavior and anisotropy of the investigated magnesium alloys: texture weakening, grain size reduction, and precipitation strengthening.

As a result, the Mg2Nd series, which had high yield strengths and was symmetrical in compression and tension, resulting in an SDE close to 0, could be extruded. Thus, products with a wide variety of yield strengths (CYS −105 to −197 MPa, TYS 107 to 203 MPa) and good ductility, with elongation to failures of −0.18 to −0.32 in compression and 0.17 to 0.41 in tension tests, were obtained. The YSs of the Mg2Yb alloy are below those of the Mg2Nd alloy and range from −58 to −111 MPa for the CYS and 89 to 115 MPa for the TYS, with similarly high elongations to failure between −0.22 and −0.3 in compression and 0.21 and 0.32 in tensile tests.

By adjusting the extrusion parameters, the grain size of the Mg2Nd alloy can be gradually reduced, thereby significantly increasing the strength. The texture of the A- and B-series effectively suppresses TTW-ing. At the beginning of compressive and tensile deformation, similar deformation mechanisms are active. This leads to a symmetrical yielding behavior and SDEs close to zero. A slower extrusion speed decreases the grain size and weakens the texture. The appearance of a <10.0> texture component in the C-series promotes TTW-ing during compression. However, because of the small grain size, CYS and TYS are similar and the SDE remains at 0. The precipitation state can be changed by subsequent heat treatment, which, in turn, further increases the yield strengths while maintaining good ductility.

Depending on the extrusion parameters, the Mg2Yb series tend to have larger grain sizes and less pronounced rare earth textures. This leads to intensive TTW-ing under compressive stress, resulting in high SDEs. Subsequent heat treatments can increase the YS. Since the effect on the slip systems is stronger than on the formation of TTWs, this leads to further increased SDEs. However, by reducing the extrusion temperature the grain size of the Mg2Yb alloy is also reduced and an advantageous texture can be achieved. This is accompanied by a significant increase in YS. Since $CRSS_{ttw}$ in particular is very sensitive to grain size, the CYS increases more than the TYS. Therefore, it is also possible to obtain an SDE close to 0 for the Mg2Yb alloy.

Supplementary Materials: The following are available online at https://www.mdpi.com/2075-4701/11/3/377/s1: Figure S1: Cross sections of the A- and B-series of the Mg2Nd and Mg2Yb alloy at different strains and elongation to failure. Figure S2: Comparison of the measured and simulated texture development during deformation of the A- and B-series of the Mg2Nd and Mg2Yb alloy at different strains. Figure S3: Comparison of the flow curves from compression and tensile tests of the A-, B- and C-series of the Mg2Nd and Mg2Yb alloy. Figure S4: Comparison of the experimentally measured and simulated axial elastic lattice strains during (a, b) compression and (c, d) tensile tests of the A- and B-series of the Mg2Nd alloy. Figure S5: Comparison of the experimentally measured and simulated axial elastic lattice strains during (a, b) compression and (c, d) tensile tests of the A- and B-series of the Mg2Yb alloy. Figure S6: Deformation mode activity as a function of strain of the A- and B-series of the Mg2Nd alloy. Figure S7: CRSS of the different deformation systems as a function of strain of the A- and B-series of the Mg2Nd alloy. Figure S8: Deformation mode activity as a function of strain of the A- and B-series of the Mg2Yb alloy. Figure S9: CRSS of the different deformation systems as a function of strain of the A- and B-series of the Mg2Yb alloy.

Author Contributions: Conceptualization, J.S., I.J.B., W.R.; methodology, J.S., I.J.B.; software, J.S., I.J.B., M.K.; validation, J.S., I.J.B., W.R.; formal analysis, J.S., I.J.B.; investigation, J.S.; resources, I.J.B., W.R.; data curation, J.S., I.J.B.; writing—original draft preparation, J.S.; writing—review and editing, I.J.B., M.K., W.R.; visualization, J.S, I.J.B.; supervision, W.R.; project administration, J.S., I.J.B., W.R.; funding acquisition, W.R. All authors have read and agreed to the published version of the manuscript.

Conflicts of Interest: The authors declare no conflict of interest. The funders had no role in the design of the study; in the collection, analysis, or interpretation of data; in the writing of the manuscript; or in the decision to publish the results.

References

1. Zeng, Z.; Stanford, N.; Davies, C.H.J.; Nie, J.-F.; Birbilis, N. Magnesium extrusion alloys: A review of developments and prospects. *Int. Mater. Rev.* **2019**, *64*, 27–62. [CrossRef]
2. Mordike, B.; Ebert, T. Magnesium. *Mater. Sci. Eng. A* **2001**, *302*, 37–45. [CrossRef]
3. Gupta, M.; Sharon, N.M.L. *Magnesium, Magnesium Alloys, and Magnesium Composites*; Wiley: Hoboken, NJ, USA, 2011; ISBN 9780470494172.
4. Friedrich, H.E.; Mordike, B.L. *Magnesium Technology*; Springer: Berlin/Heidelberg, Germany, 2006; ISBN 3-540-20599-3.
5. Arul Kumar, M.; Beyerlein, I.J.; Tomé, C.N. A measure of plastic anisotropy for hexagonal close packed metals: Application to alloying effects on the formability of Mg. *J. Alloy. Compd.* **2017**, *695*, 1488–1497. [CrossRef]
6. Chelladurai, I.; Miles, M.P.; Fullwood, D.T.; Carsley, J.E.; Mishra, R.K.; Beyerlein, I.J.; Knezevic, M. Microstructure Correlation with Formability for Biaxial Stretching of Magnesium Alloy AZ31B at Mildly Elevated Temperatures. *JOM* **2017**, *69*, 907–914. [CrossRef]
7. Clausen, B.; Tomé, C.N.; Brown, D.W.; Agnew, S.R. Reorientation and stress relaxation due to twinning: Modeling and experimental characterization for Mg. *Acta Mater.* **2008**, *56*, 2456–2468. [CrossRef]
8. Hutchinson, W.B.; Barnett, M.R. Effective values of critical resolved shear stress for slip in polycrystalline magnesium and other hcp metals. *Scr. Mater.* **2010**, *63*, 737–740. [CrossRef]
9. Ion, S.E.; Humphreys, F.J.; White, S.H. Dynamic recrystallisation and the development of microstructure during the high temperature deformation of magnesium. *Acta Metall.* **1982**, *30*, 1909–1919. [CrossRef]
10. Yoo, M.H. Slip, twinning, and fracture in hexagonal close-packed metals. *MTA* **1981**, *12*, 409–418. [CrossRef]
11. Liu, B.-Y.; Liu, F.; Yang, N.; Zhai, X.-B.; Zhang, L.; Yang, Y.; Li, B.; Li, J.; Ma, E.; Nie, J.-F.; et al. Large plasticity in magnesium mediated by pyramidal dislocations. *Science* **2019**, *365*, 73–75. [CrossRef]
12. Yoo, M.H.; Lee, J.K. Deformation twinning in h.c.p. metals and alloys. *Philos. Mag. A* **1991**, *63*, 987–1000. [CrossRef]
13. Beyerlein, I.J.; Zhang, X.; Misra, A. Growth Twins and Deformation Twins in Metals. *Annu. Rev. Mater. Res.* **2014**, *44*, 329–363. [CrossRef]
14. Kumar, M.A.; Beyerlein, I.J. Local microstructure and micromechanical stress evolution during deformation twinning in hexagonal polycrystals. *J. Mater. Res.* **2020**, *35*, 217–241. [CrossRef]
15. Knezevic, M.; Beyerlein, I.J. Multiscale Modeling of Microstructure-Property Relationships of Polycrystalline Metals during Thermo-Mechanical Deformation. *Adv. Eng. Mater.* **2018**, *20*, 1700956. [CrossRef]
16. Christian, J.W.; Mahajan, S. Deformation twinning. *Prog. Mater. Sci.* **1995**, *39*, 1–157. [CrossRef]
17. Stanford, N.; Atwell, D.; Beer, A.; Davies, C.; Barnett, M.R. Effect of microalloying with rare-earth elements on the texture of extruded magnesium-based alloys. *Scr. Mater.* **2008**, *59*, 772–775. [CrossRef]
18. Barnett, M.R. Twinning and the ductility of magnesium alloys. *Mater. Sci. Eng. A* **2007**, *464*, 1–7. [CrossRef]
19. Hirth, J.P.; Cohen, M. On the strength-differential phenomenon in hardened steel. *Metall. Trans.* **1970**, *1*, 3–8. [CrossRef]
20. Spitzig, W.; Sober, R.; Richmond, O. Pressure dependence of yielding and associated volume expansion in tempered martensite. *Acta Metall.* **1975**, *23*, 885–893. [CrossRef]
21. Stanford, N.; Barnett, M.R. The origin of "rare earth" texture development in extruded Mg-based alloys and its effect on tensile ductility. *Mater. Sci. Eng. A* **2008**, *496*, 399–408. [CrossRef]
22. Stanford, N.; Barnett, M. Effect of composition on the texture and deformation behaviour of wrought Mg alloys. *Scr. Mater.* **2008**, *58*, 179–182. [CrossRef]
23. Lentz, M.; Klaus, M.; Coelho, R.S.; Schaefer, N.; Schmack, F.; Reimers, W.; Clausen, B. Analysis of the Deformation Behavior of Magnesium-Rare Earth Alloys Mg-2 pct Mn-1 pct Rare Earth and Mg-5 pct Y-4 pct Rare Earth by In Situ Energy-Dispersive X-ray Synchrotron Diffraction and Elasto-Plastic Self-Consistent Modeling. *Metall. Mater. Trans. A* **2014**, *45*, 5721–5735. [CrossRef]
24. Lentz, M.; Klaus, M.; Wagner, M.; Fahrenson, C.; Beyerlein, I.J.; Zecevic, M.; Reimers, W.; Knezevic, M. Effect of age hardening on the deformation behavior of an Mg–Y–Nd alloy: In-situ X-ray diffraction and crystal plasticity modeling. *Mater. Sci. Eng. A* **2015**, *628*, 396–409. [CrossRef]

25. Bohlen, J.; Yi, S.; Letzig, D.; Kainer, K.U. Effect of rare earth elements on the microstructure and texture development in magnesium–manganese alloys during extrusion. *Mater. Sci. Eng. A* **2010**, *527*, 7092–7098. [CrossRef]

26. Seitz, J.-M.; Eifler, R.; Stahl, J.; Kietzmann, M.; Bach, F.-W. Characterization of MgNd2 alloy for potential applications in bioresorbable implantable devices. *Acta Biomater.* **2012**, *8*, 3852–3864. [CrossRef] [PubMed]

27. Turner, P.A.; Tomé, C.N. A study of residual stresses in Zircaloy-2 with rod texture. *Acta Metall. Et Mater.* **1994**, *42*, 4143–4153. [CrossRef]

28. Zecevic, M.; Knezevic, M.; Beyerlein, I.J.; Tomé, C.N. An elasto-plastic self-consistent model with hardening based on dislocation density, twinning and de-twinning: Application to strain path changes in HCP metals. *Mater. Sci. Eng. A* **2015**, *638*, 262–274. [CrossRef]

29. Rokhlin, L.L. *Magnesium Alloys Containing Rare Earth Metals*; CRC Press: London, UK, 2003; ISBN 9780429179228.

30. Bachmann, F.; Hielscher, R.; Schaeben, H. Texture Analysis with MTEX—Free and Open Source Software Toolbox. *Solid State Phenom.* **2010**, *160*, 63–68. [CrossRef]

31. Klaus, M.; Garcia-Moreno, F. The 7T-MPW-EDDI beamline at BESSY II. *JLSRF* **2016**, *2*. [CrossRef]

32. Genzel, C.; Denks, I.A.; Coelho, R.; Thomas, D.; Mainz, R.; Apel, D.; Klaus, M. Exploiting the features of energy-dispersive synchrotron diffraction for advanced residual stress and texture analysis. *J. Strain Anal. Eng. Des.* **2011**, *46*, 615–625. [CrossRef]

33. Beyerlein, I.J.; Knezevic, M. Mesoscale, Microstructure-Sensitive Modeling for Interface-Dominated, Nanostructured Materials. In *Handbook of Materials Modeling*; Andreoni, W., Yip, S., Eds.; Springer International Publishing: Cham, Switzerland, 2020; pp. 1111–1152. ISBN 978-3-319-44676-9.

34. Wang, J.; Zecevic, M.; Knezevic, M.; Beyerlein, I.J. Polycrystal plasticity modeling for load reversals in commercially pure titanium. *Int. J. Plast.* **2020**, *125*, 294–313. [CrossRef]

35. Beyerlein, I.J.; Tomé, C.N. A dislocation-based constitutive law for pure Zr including temperature effects. *Int. J. Plast.* **2008**, *24*, 867–895. [CrossRef]

36. Knezevic, M.; Beyerlein, I.J.; Brown, D.W.; Sisneros, T.A.; Tomé, C.N. A polycrystal plasticity model for predicting mechanical response and texture evolution during strain-path changes: Application to beryllium. *Int. J. Plast.* **2013**, *49*, 185–198. [CrossRef]

37. Proust, G.; Tomé, C.N.; Kaschner, G.C. Modeling texture, twinning and hardening evolution during deformation of hexagonal materials. *Acta Mater.* **2007**, *55*, 2137–2148. [CrossRef]

38. Nie, J.-F. Precipitation and Hardening in Magnesium Alloys. *MTA* **2012**, *43*, 3891–3939. [CrossRef]

39. Lefebvre, W.; Kopp, V.; Pareige, C. Nano-precipitates made of atomic pillars revealed by single atom detection in a Mg-Nd alloy. *Appl. Phys. Lett.* **2012**, *100*, 141906. [CrossRef]

40. Dobromyslov, A.V.; Kaigorodova, L.I.; Sukhanov, v.d.; Dobatkina, T.V. Decomposition of a supersaturated solid solution in the Mg-3.3 wt% Yb alloy. *Phys. Met. Met.* **2007**, *103*, 64–71. [CrossRef]

41. Dobroň, P.; Chmelík, F.; Yi, S.; Parfenenko, K.; Letzig, D.; Bohlen, J. Grain size effects on deformation twinning in an extruded magnesium alloy tested in compression. *Scr. Mater.* **2011**, *65*, 424–427. [CrossRef]